

# Magnetic Properties of YbBe<sub>13</sub> Probed by Neutron Scattering and Thermodynamic Measurements

Yusei Shimizu<sup>\*1</sup>, Yoichi Ikeda<sup>2</sup>, Toshiro Sakakibara<sup>3</sup>, Yoshiya Homma<sup>1</sup>, and Dai Aoki<sup>1</sup>

<sup>1</sup>Institute for Materials Research (IMR), Tohoku University, Oarai, Ibaraki, 311-1313, Japan

<sup>2</sup>Institute for Materials Research (IMR), Tohoku University, Sendai, Miyagi, 980-8577, Japan

<sup>3</sup>Institute for Solid State Physics (ISSP), University of Tokyo, Kashiwa, Chiba 277-8581, Japan

We examined the magnetic properties of YbBe<sub>13</sub>, which exhibits an antiferromagnetic order below  $T_N \sim 1.2$  K. Unlike other  $M\text{Be}_{13}$  compounds ( $M = \text{rare earth/actinide elements}$ ), based on elastic neutron scattering, we observed an incommensurate magnetic propagation vector  $\tau = (0, 0, \tau_z)$ , where  $\tau_z = 0.5385$  is in the reciprocal lattice unit. Additionally, we constructed a precise magnetic phase diagram for YbBe<sub>13</sub>. We observed non-trivial magnetic anomalies in YbBe<sub>13</sub>, which cannot be understood based on a simple helical order. Our results for YbBe<sub>13</sub> provide an opportunity to reconsider the electron state of UBe<sub>13</sub> and present an important step toward a comprehensive understanding of magnetic correlations in  $M\text{Be}_{13}$  series.

The  $M\text{Be}_{13}$  ( $M = \text{U, Th, Np, and rare-earth elements}$ ) series with cubic  $\text{NaZn}_{13}$  structure (space group: #226,  $O_h^6$ ) exhibits various physical properties and has been extensively investigated.<sup>1,2</sup> Among them, UBe<sub>13</sub> is of particular interest as it is a system with delocalized  $f$  electrons exhibiting extremely strong electron correlations. It shows unconventional superconductivity,<sup>2</sup> magnetic anomalies ( $B^*$  anomaly) in the superconducting state,<sup>3-5</sup> and non-Fermi-liquid behavior.<sup>6-8</sup> Although UBe<sub>13</sub> is a promising candidate for spin-triplet superconductors,<sup>9,10</sup> its  $B^*$  anomaly may be originated from a short-range spin-density-wave (SDW) state.<sup>4</sup> In addition, although a magnetic correlation of  $(\frac{1}{2}, \frac{1}{2}, 0)$  has been observed in UBe<sub>13</sub>,<sup>11-13</sup> no microscopic picture reflecting the relationship between magnetic correlations and superconductivity has been obtained.

In order to understand the basic magnetic correlations in UBe<sub>13</sub> with extremely strongly-correlated electron state, it is also important to investigate the detailed magnetic structure of  $M\text{Be}_{13}$  in a weakly correlated electron regime. The  $M\text{Be}_{13}$  series tend to exhibit helical magnetism with a propagation vector of  $\tau = (0, 0, \frac{1}{3})$  ( $M = \text{Np, Dy, and Ho}$ )<sup>14-16</sup> and a slightly modified incommensurate ordering with  $\tau = (0, 0, 0.285)$  for GdBe<sub>13</sub>,<sup>17</sup> when the  $f$ -electrons are localized.

In this study, we utilize a promising candidate, YbBe<sub>13</sub>, to understand the fundamentals of the magnetic ground and electronic states when localized  $f$  electrons acquire itinerancy in the  $M\text{Be}_{13}$  series. We address the magnetic structure of YbBe<sub>13</sub>, which has been reported to exhibit an antiferromagnetic order below  $T_N \sim 1.15\text{-}1.28$  K.<sup>18,19</sup> In the paramagnetic state, the magnetic susceptibility,  $\chi(T)$ , obeys the Curie-Weiss law for the Yb<sup>3+</sup> state, where the Curie-Weiss temperature  $\theta$  is approximately 1 K.<sup>18</sup> The isomer shift evaluated from Mössbauer spectroscopy measurements also revealed that Yb is in the trivalent state ( $J = 7/2$ ) with Ruderman-Kittel-Kasuya-Yosida interaction,<sup>20</sup> although the possibility of a mixed valent state for Yb ion was discussed in an earlier paper.<sup>21</sup> However, x-ray absorption results reported that Yb ion has a trivalent state in the bulk YbBe<sub>13</sub>.<sup>22</sup> In YbBe<sub>13</sub>, the crystalline-electric-field (CEF) state of the  $4f$  electrons can be well understood from inelastic-neutron scattering<sup>23</sup> and heat-capacity measurements,<sup>19</sup> which suggest CEF levels of  $\Gamma_7\text{-}$

$\Gamma_8\text{-}\Gamma_6$ , where  $\Gamma_7$ ,  $\Gamma_8$  and  $\Gamma_6$  are the CEF ground, first-excited, and second-excited states, respectively. This indicates that  $f$  electrons in YbBe<sub>13</sub> are localized. However, the occurrence of the Kondo effect in YbBe<sub>13</sub>, as suggested by the Mössbauer effect<sup>20</sup> and heat-capacity experiments,<sup>19</sup> implies that the  $f$  electrons are itinerant, with a moderate effective mass at low temperatures ( $\gamma \sim 30 \text{ J K}^{-2} \text{ mol}^{-1}$ ).

To clarify the magnetic structure of YbBe<sub>13</sub> in the antiferromagnetic order, we performed elastic neutron-scattering, DC magnetization, and specific-heat measurements using single-crystalline samples. Based on elastic neutron-scattering measurements, we propose possible magnetic structures below  $T_N \sim 1.2$  K, which have an incommensurate propagation vector of  $\tau = (0, 0, 0.5385)$ . Additionally, we present a non-trivial magnetic phase diagram for YbBe<sub>13</sub>.

Single-crystalline YbBe<sub>13</sub> samples were grown via the Al flux method using alumina crucibles in a sealed quartz tube. After centrifuging the Al flux, the flux on the crystal surface was removed using NaOH solution. No sample dependence was observed for single crystals obtained from the same batch.

Elastic neutron-scattering profiles were measured using a triple-axis neutron spectrometer TOPAN installed on the 6G horizontal beam port in JRR-3. The incident and scattered neutrons were monochromatized with pyrolytic graphite (PG) (002) crystals and calibrated to  $\lambda = 246.7$  pm ( $\sim 13.4$  meV) using an  $\alpha$ -alumina standard sample. The monochromator and analyzer were vertically focused, and collimators (30'-30'-30'-60') were used before and after they were placed. High-order harmonics were reduced using PG filters. Small single crystals (total weight: 42 mg) were fixed on an aluminum plate using hydrogen-free glue (CYTOP). Each crystal was coaligned such that the horizontal scattering plane was ( $hhl$ ). A closed-cycle <sup>3</sup>He refrigerator was used to cool the samples to 0.69 K. The mosaic of the coaligned samples was coarse and evaluated to be a few degrees. Therefore, we focused only on determining the magnetic reflections of YbBe<sub>13</sub>.

Low-temperature magnetization measurements were performed using the Faraday method. We used a high-resolution capacitively detected magnetometer<sup>24,25</sup> installed in a <sup>3</sup>He refrigerator at low temperatures down to 0.28 K under magnetic fields along the cubic  $\langle 100 \rangle$  axis for a single-crystalline sam-

\*E-mail address: yusei.shimizu.a5@tohoku.ac.jp

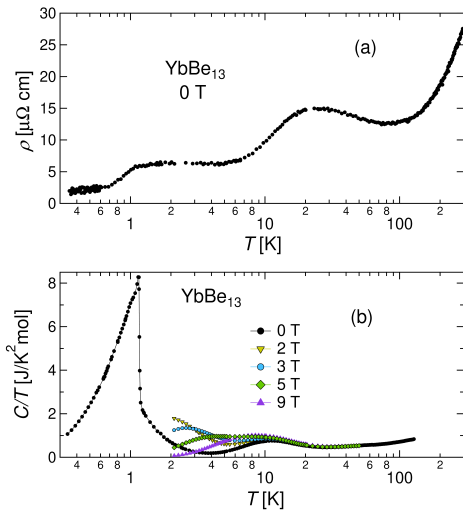


Fig. 1. (a) Temperature dependence of resistivity in  $\text{YbBe}_{13}$  (logarithmic temperature scale), where the residual-resistivity ratio was 15. (b) Temperature dependence of heat capacity  $[C(T)/T]$  in  $\text{YbBe}_{13}$  from 130 K to the lowest temperature of 0.34 K (logarithmic temperature scale). We also plot  $C(T)/T$  data below 50 K at 2, 3, 5, and 9 T along the  $\langle 100 \rangle$  axis.

ple weighing 2.68 mg. We examined the difference between the field-cooling and zero-field-cooling processes for the antiferromagnetic order in  $\text{YbBe}_{13}$  but did not observe significant differences between them.

Meanwhile, heat-capacity and resistivity measurements were performed using a commercial Physical Properties Measurement Systems (PPMS Dynacool, Quantum Design) at low temperatures down to 0.34 K. For heat-capacity measurements, we applied magnetic fields up to 9 T along the cubic  $\langle 100 \rangle$  axis. We measured the electrical resistivity via the four-probe method using gold wires; subsequently, the resistivity value was normalized using a previously reported value in the literature.<sup>26)</sup>

First, we report the transport and thermophysical properties of a single-crystalline  $\text{YbBe}_{13}$  sample. Figures 1(a) and 1(b) show the temperature dependences (logarithmic temperature scale) of the resistivity and heat capacity, respectively. The resistivity decreases upon cooling from room temperature to 70 K, and there is a broad maximum at 20–30 K under zero field. In the low temperature region below 20 K, the variation of  $\rho(T)$  with respect to temperature was insignificant down to 2 K. At 1.18 K, a kink behavior was clearly observed in  $\rho(T)$ , which was due to the antiferromagnetic transition in  $\text{YbBe}_{13}$ . These behaviors are consistent with previous resistivity measurements.<sup>26, 27)</sup> Meanwhile, the  $\rho(T)$  data suggest that the 4*f* electrons in  $\text{YbBe}_{13}$  are not in a strongly correlated regime, as  $\rho(T)$  varies weakly and the value of *A* coefficient is very small at low temperatures.

In the heat-capacity data measured at zero field, a broad local maximum was observed at 10 K, which is approximately half the value of the resistivity maximum temperature. There is no sample dependence for the observed broad maximum behavior in the resistivity and heat capacity of the single-crystalline samples. Meanwhile,  $C(T)/T$  exhibited a large  $\lambda$ -shaped anomaly at  $T_N \sim 1.2$  K owing to the antiferromagnetic transition, thus suggesting a second-order phase transition. Above  $T_N$ , a large enhancement in  $C/T$  is observed, pre-

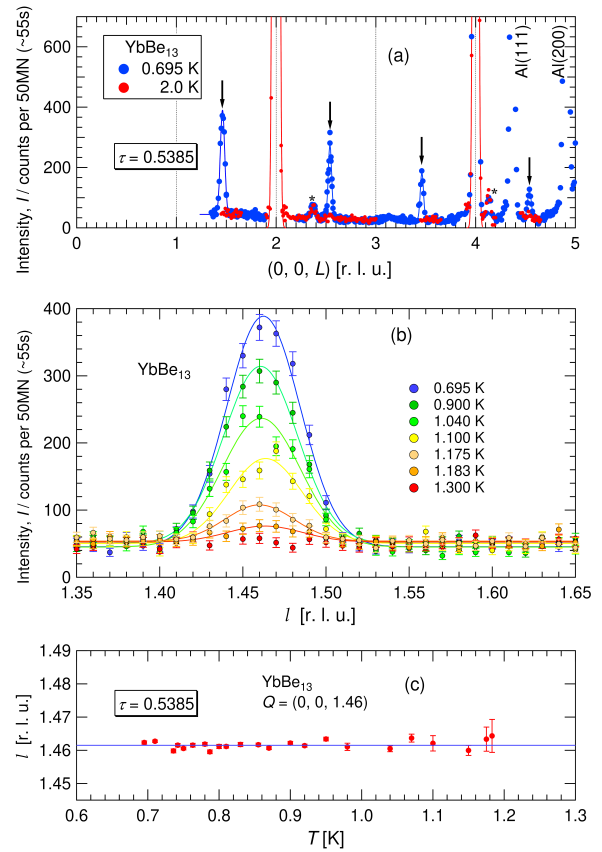


Fig. 2. (a) The line scan profile along  $(00L)$  measured at the base temperature, 0.695 K (blue circles) in the magnetic ordered state, and 2 K in the paramagnetic state (red circles). (b) Temperature dependence of elastic neutron-scattering intensity at  $\mathbf{Q} = (0, 0, 1.46)$  as a function of  $l$  r.l.u. (c) Temperature dependence of the peak centers at around  $\mathbf{Q} = (0, 0, 1.46)$ , where there is no change in the center of the magnetic Bragg peak within the experimental accuracy.

sumably owing to antiferromagnetic fluctuations. The heat-capacity data obtained under magnetic fields up to 9 T were plotted, as shown in Fig. 1(b). The broad anomaly at 10 K varied significantly under the applied magnetic fields. Moreover, an additional peak anomaly appeared at 3–4 K at 3 and 5 T. Previous inelastic neutron-scattering<sup>23)</sup> and heat-capacity<sup>19)</sup> studies suggested that the CEF ground state is the  $\Gamma_7$  doublet, whereas the first and second excited states are the  $\Gamma_8$  quartet and  $\Gamma_6$  doublet, respectively. The field-induced anomaly observed at 3 and 5 T may originate from the Schottky anomaly with a splitting of the  $\Gamma_7$  ground state in the magnetic field.

Next, we report the results of elastic neutron-scattering measurements for  $\text{YbBe}_{13}$ . Several line scans were performed to determine the magnetic reflections below  $T_N$ . A typical line-scan profile is shown in Fig. 2(a). The blue and red points were measured at 0.695 K (below  $T_N$ ) and 2 K (above  $T_N$ ), respectively. The intense peaks around  $l = 2$  and 4 r. l. u. are the fundamental nuclear reflections from  $\text{YbBe}_{13}$ , whereas those around  $l \sim 4.3$  and 4.8 r. l. u. are background Bragg reflections from the aluminum cell. Additionally, the temperature-independent small peaks around  $l \sim 2.4$  and 4.1 r. l. u. are spurious scatterings from the refrigerator. The absence of clear Bragg reflections at  $\mathbf{Q} = (0, 0, 2n + 1)$ , where  $n$  is an integer, is consistent with the face-centered cubic structure of  $\text{YbBe}_{13}$  (space group #226,  $Fm\bar{3}c$ ). At the base temperature,

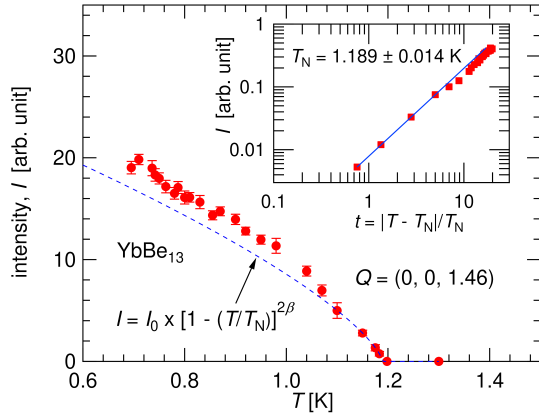


Fig. 3. Neutron-scattering intensity ( $I$ ) in  $\text{YbBe}_{13}$  at  $\mathbf{Q} = (0, 0, 1.46)$  as a function of temperature. The dashed line is the result of a fit with  $I = I_0 \times [1 - (T/T_N)]^{2\beta}$ , where  $T_N = 1.189$  K and  $\beta = 0.36$ . The inset shows the log-log plot of  $I$  versus the reduced temperature  $t \equiv |T - T_N|/T_N$ .

clear satellite peaks are observed around the (002) and (004) planes, as indicated by the downward black arrows in Fig. 2(a). These satellites can be expressed as  $\mathbf{Q} = \mathbf{G} \pm \boldsymbol{\tau}$ , where  $\mathbf{G}$  is the reciprocal lattice vector of  $\text{YbBe}_{13}$  and  $\boldsymbol{\tau} = (0, 0, \tau_z)$  is the magnetic propagation wave vector. To evaluate  $\tau_z$ , the observed peaks were fitted with a Gaussian function, and  $\tau_z$  was evaluated to be  $0.5385 \pm 0.0003$  r.l.u. at the base temperature. This incommensurate propagation vector in  $\text{YbBe}_{13}$  differs completely from that of the commensurate magnetism in  $M\text{Be}_{13}$  ( $M = \text{Dy}, \text{Ho}, \text{and Np}$ ).<sup>14–16)</sup>

To determine whether the observed peak is due to a magnetic transition, we examined the temperature evolution of the peak intensity near  $\mathbf{Q} = (0, 0, 1.46)$ . As shown in Fig. 2(b), the observed peak became smaller with increasing temperature and fully disappeared at  $T = 1.3$  K (above  $T_N$ ). Furthermore, the observed intensity shown in Fig. 2(a) decreased as the scattering vector increased. The  $\mathbf{Q}$  dependence can be interpreted as the effect of the magnetic form factor of the Yb ions. These results indicate that the observed satellites are most likely due to the magnetic transition below  $T \sim 1.2$  K, which is consistent with the results of  $\rho(T)$  and  $C(T)$ .

Figure 3 shows the temperature dependence of the neutron-scattering intensity at  $\mathbf{Q} = (0, 0, 1.46)$  for  $\text{YbBe}_{13}$ . The neutron intensity ( $I$ ) clearly developed below  $T \sim 1.2$  K, which is consistent with the heat-capacity results [Fig. 1(b)]. The dashed line presents the fitting between 1.1 and 1.2 K with an empirical formula,  $I = I_0 \times [1 - (T/T_N)]^{2\beta}$ , where  $T_N = 1.189 \pm 0.014$  K and  $\beta = 0.36 \pm 0.25$ . The inset shows  $I$  vs. the reduced temperature  $t \equiv |T - T_N|/T_N$  in the logarithmic scale. The neutron-scattering intensity is generally proportional to the volume of the specimen ( $V$ ) and the square of the ordered magnetic moment ( $m^2$ ), i.e.,  $I \propto Vm^2$ . In the case of mean-field approximation,  $\beta$  is 0.5, whereas it is 0.35 and 0.36 for the  $XY$  and three-dimensional Heisenberg models, respectively.<sup>28)</sup> These values of  $\beta$  are not significantly different from the experimentally determined value.

The possible magnetic structures can be listed via an irreducible representation analysis based on the evaluated propagation vector.<sup>29,30)</sup> For  $\text{YbBe}_{13}$ , only three types of mag-

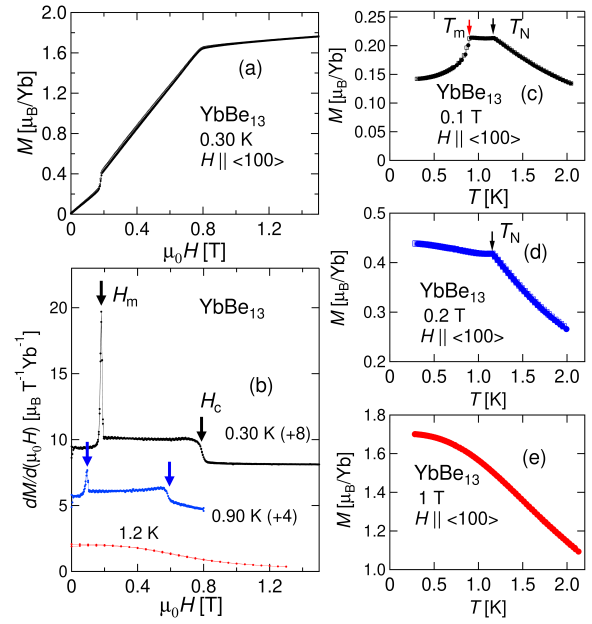


Fig. 4. (a) Magnetization process of  $\text{YbBe}_{13}$ , measured in magnetic fields applied along the cubic  $\langle 100 \rangle$  axis. (b) Differential magnetization of  $\text{YbBe}_{13}$ ,  $dM/dH$ , measured at 0.30, 0.90, and 1.2 K. Here, the data measured at 0.30 and 0.90 K are shifted vertically for the clarity, where the values are denoted in parentheses. Temperature dependence of magnetization, measured at (c) 0.1, (d) 0.2, and (e) 1 T, for  $H \parallel \langle 100 \rangle$ .

netic structures can be realized just below  $T_N$  for  $\boldsymbol{\tau} = (0, 0, 0.5385)$ . Two of these exhibit longitudinal sinusoidal modulations along the [001] axis. The third type is helicoidal modulation, in which the magnetic moments are perpendicular to the propagation vector ([001] axis). We will discuss the magnetically ordered state in  $\text{YbBe}_{13}$  later, in addition to the low- $T$  magnetization data.

Figure 4(a) shows the magnetization process of  $\text{YbBe}_{13}$  in magnetic fields along the cubic  $\langle 100 \rangle$  axis, measured at 0.30 K. A clear step-like behavior is observed in  $M(H)$  at  $\mu_0 H_m = 0.18$  T, and a kink appears at  $\mu_0 H_c = 0.8$  T. Above 0.18 T, the magnetization curve is almost linear with  $H$  below  $\mu_0 H_c = 0.8$  T. An anomaly is observed at  $H_c$  in both the increasing and decreasing field processes, thus implying a phase transition. In this study, we performed magnetization measurements under fields up to 6 T; however, no anomalies were observed above  $H_c$ . Figure 4(b) shows the differential magnetization [ $dM(H)/dH$ ] curves obtained at 0.30, 0.60, and 1.2 K. The sharp cusp in  $dM(H)/dH$  at  $H_m$  indicates a first-order transition. Meanwhile, the step-like behavior in  $dM(H)/dH$  at  $\mu_0 H_c = 0.8$  T (0.6 T) for 0.30 K (0.90 K) suggests a second-order phase transition at  $H_c$ .

Next, we examined the temperature dependence of the magnetization [ $M(T)$ ]. Figures 4(c), 4(d), and 4(e) show  $M(T)$ , measured at 0.1, 0.2, and 1 T, respectively. At 0.1 T, a distinct anomaly below 1 K is apparent, which is denoted as  $T_m$  [Fig. 4(c)], in both the increasing and decreasing processes. This behavior is consistent with the magnetic-field dependence of  $M(H)$ . At 0.2 T, such behavior was not observed below  $T_N$ . At 1 T, which is higher than the critical field ( $H_c$ ) of the antiferromagnetic order in  $\text{YbBe}_{13}$ , no anomalies were

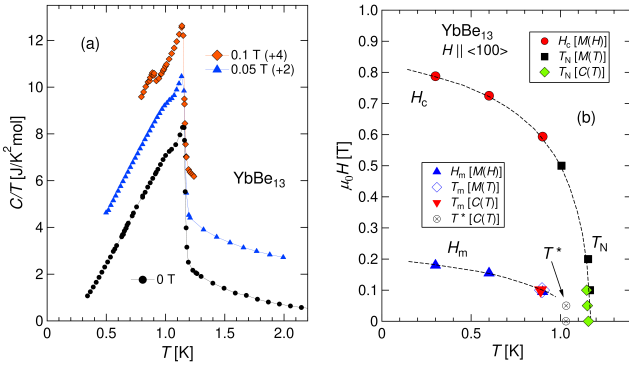


Fig. 5. (a) The temperature dependence of heat capacity in single crystalline  $\text{YbBe}_{13}$ , measured at zero and magnetic fields, 0.05 and 0.1 T applied along the cubic  $\langle 100 \rangle$  axis. Here, the data measured in magnetic fields are shifted vertically for the clarity, where the values are denoted in parentheses. (b) The obtained  $H$ - $T$  phase diagram in  $\text{YbBe}_{13}$  for  $H \parallel \langle 100 \rangle$ . The details are explained in the text.

observed in  $M(T)$ .

Figure 5(a) shows the temperature dependence of the heat capacity measured at zero and under magnetic fields of 0.05 and 0.1 T. At zero field, a large peak was observed at  $T_N \sim 1.2$  K owing to the antiferromagnetic transition. The observed behavior is similar to that reported previously for heat capacity.<sup>19)</sup> However, in previous studies, shoulder-like anomalies at  $\sim 0.9$ -1 K were not very evident. In this study, we observed a shoulder-like anomaly ( $T^* \sim 0.9$ -1 K) under a very low field below 0.05 T, which is likely a crossover anomaly in the antiferromagnetic phase. Notably, the relationship among  $H_m$ ,  $T^*$ , and  $T_N$  in the  $H$ - $T$  phase diagram of  $\text{YbBe}_{13}$  is worth investigating in future studies.

Figure 5(b) shows the  $H$ - $T$  phase diagram of  $\text{YbBe}_{13}$  for  $H \parallel \langle 100 \rangle$ . The open circles, squares, and diamonds represent the critical fields of antiferromagnetic order in  $\text{YbBe}_{13}$  obtained from the magnetization process [ $M(H)$ ], the temperature dependence of magnetization [ $M(T)$ ], and the temperature dependence of the heat capacity, respectively. Additionally, we plotted the corresponding anomalies inside the antiferromagnetic phase, as denoted by  $M(H)$  (triangles),  $M(T)$  (diamonds), and  $C(T)/T$  (circles with crosses). In the low-field region, anomalies were evident in the field and temperature dependences of the magnetization, which are denoted as  $H_m$  and  $T_m$ , respectively. This low-field anomaly can be similarly explained based on  $C(T)/T$  data at 0.1 T [Fig. 5(b)].

Having established that the magnetic order in  $\text{YbBe}_{13}$  has a propagation vector of  $\tau = (0, 0, 0.5385)$ , we now discuss the behavior of the magnetization curve for  $\text{YbBe}_{13}$ . In a cubic system, three equivalent domains with propagation vectors of  $(\tau_x, 0, 0)$ ,  $(0, \tau_y, 0)$ , and  $(0, 0, \tau_z)$  should exist at zero field. Such a multi-domain state is destabilized in a finite magnetic field because of the non-equivalent Zeeman effect between the parallel and orthogonal domains.<sup>31)</sup> In  $\text{GdBe}_{13}$ , a multi-domain state was discussed in the low-field region of its helical order.<sup>32)</sup> By contrast, a change in the domain structure cannot explain the  $M(H)$  data of  $\text{YbBe}_{13}$  because the anomaly at  $H_m$  is evident in the field-decreasing process of  $M(H)$  [Fig. 4(a)], unlike in the case of  $\text{GdBe}_{13}$ .

Hence, a plausible explanation for the observed anomalies at  $H_m$  and  $T_m$  is a change in the magnetic structure of  $\text{YbBe}_{13}$ .

In the case of helical order with  $\tau = (0, 0, 0.5385)$  with a helical (001) planes, the helical state becomes a conical state with a linear  $M(H)$  curve, unlike the case for the experimental  $M(H)$  data in  $\text{YbBe}_{13}$ . Although the linear  $M(H)$  curve in  $\text{YbBe}_{13}$  above  $H_m$  is similar to that of helical magnetic systems,<sup>32-35)</sup> the low-field ordered state below the first-order transition at  $H_m$  cannot be explained by a simple helical order. The determination of the precise magnetic structure of  $\text{YbBe}_{13}$  is currently in progress.

Under 0.05 T and zero field, a shoulder-like anomaly was observed at  $T^* \sim 1$  K in  $C(T)/T$  curves [Figs. 5(a) and 5(b)]. The entropy change for this anomaly is very small. Therefore, a significant change in the magnetic structure may be excluded at  $T^*$ . In connection with this weak anomaly, no clear sign is observed in the resistivity within the experimental accuracy. Although the temperature evolution of the neutron-scattering intensity was reproduced approximately using the empirical equation, the neutron-scattering intensity at  $\mathbf{Q} = (0, 0, 1.46)$  appeared to be slightly enhanced below 1 K (Fig. 3), at which the neutron intensity  $I$  deviated from the critical behavior in the log-log plot (inset of Fig. 3). Hence, the modification of the magnetic structure due to the slight change in the coefficients of the linear combination for the basis vectors might cause the weak anomaly at  $T^*$  in  $\text{YbBe}_{13}$ . In fact, an enigmatic helical magnetic structure with sine modulation in  $\text{NpBe}_{13}$  suggests a complex magnetic correlation in  $M\text{Be}_{13}$ .<sup>14)</sup> In addition, based on the emergence of third-order harmonics at low temperatures, a rearrangement of the magnetic structure in  $\text{HoBe}_{13}$  has been reported.<sup>16)</sup> Further studies are necessary to understand the observed anomalies in the incommensurate order in  $\text{YbBe}_{13}$ .

Finally, we discuss the reason for the incommensurate propagation  $(0, 0, 0.5385)$  vector appearing in  $\text{YbBe}_{13}$ , which differs significantly from the commensurate vector  $(0, 0, \frac{1}{3})$  observed in other  $M\text{Be}_{13}$  compounds ( $M = \text{Np}$ ,  $\text{Dy}$ , and  $\text{Ho}$ ).<sup>14-16)</sup> An incommensurate magnetic order is a typical characteristic of the SDW state and is formed on the Fermi surface. Therefore, the Fermi surface of  $\text{YbBe}_{13}$  must be clarified and the manner by which an incommensurate magnetic correlation emerged must be elucidated. In  $\text{YbBe}_{13}$ , the characteristic resistivity  $\rho(T)$  above  $T_{\text{max}} \sim 30$  K indicates the Kondo effect [Fig. 1(a)], which is consistent with previous inelastic-neutron scattering,<sup>23)</sup> the Mössbauer effect,<sup>20)</sup> and point-contact spectroscopy experiments.<sup>36)</sup> However, the evaluated Kondo temperature  $T_K \sim 1$  K<sup>23,37)</sup> is much smaller than  $T_{\text{max}}$ , thus implying that the conduction electrons are affected by the first-excited CEF state in  $\text{YbBe}_{13}$ . Such a small  $T_K$  and the resistivity anomaly at approximately 30 K, which may be related to the CEF excited state, have been similarly observed in  $\text{UBe}_{13}$ .<sup>2)</sup> Our results for  $\text{YbBe}_{13}$  provide an opportunity to fundamentally reconsider the enigmatic  $5f$  electron state and  $B^*$  anomaly in  $\text{UBe}_{13}$ .

In summary, we examined the magnetic properties of  $\text{YbBe}_{13}$  via elastic neutron-scattering, DC magnetization and heat-capacity measurements using single-crystalline samples. Based on elastic neutron-scattering measurements, an incommensurate propagation vector  $\tau = (0, 0, 0.5385)$  was unexpectedly observed below  $T_N$ , unlike other  $M\text{Be}_{13}$  compounds. Furthermore, we obtained a non-trivial magnetic phase diagram in  $\text{YbBe}_{13}$ . Our findings for  $\text{YbBe}_{13}$  provide new insights into magnetic correlations in the  $M\text{Be}_{13}$  series when  $f$

electrons acquire an itinerant nature.

We would like to thank Manabu Okawara for technical support in JRR-3 in Tokai. The neutron scattering experiments were performed under the Joint-Use Research Program for Neutron Scattering, Institute for Solid State Physics (ISSP), University of Tokyo, at the Japan Research Reactor JRR-3 (6G IRT program 23402) and a part of the GIMRT research program in IMR (202212-CNKXX-0402). We gratefully acknowledge the support on the neutron experiments from the Center of Neutron Science for Advanced Materials, IMR, Tohoku University. This work was partly supported by Grants-in-Aid KAKENHI (No. 20K03851, 23K03314, 22KK0224, 23H04870) from the Ministry of Education, Culture, Sports, Science and Technology (MEXT) of Japan. The magnetization measurements were conducted under the Joint-Use Research Program in the Institute for Solid State Physics, the University of Tokyo.

- 1) E. Bucher, J. P. Maita, G. W. Hull, R. C. Fulton, A. S. Cooper, Phys. Rev. B **11**, 440 (1975).
- 2) H. R. Ott, H. Rudigier, Z. Fisk, and J. L. Smith, Phys. Rev. Lett. **50**, 1595 (1983).
- 3) B. Ellman, T. F. Rosenbaum, J. S. Kim, and G. R. Stewart, Phys. Rev. B **44**, 12074 (1991).
- 4) F. Kromer, R. Helfrich, M. Lang, F. Steglich, C. Langhammer, A. Bach, T. Michels, J. S. Kim, and G. R. Stewart, Phys. Rev. Lett. **81**, 4476 (1998).; F. Kromer, M. Lang, N. Oeschler, P. Hinze, C. Langhammer, F. Steglich, J. S. Kim, and G. R. Stewart, Phys. Rev. B **62**, 12477 (2000).; F. Kromer, N. Oeschler, T. Tayama, K. Tenya, T. Cichorek, M. Lang, F. Steglich, J. S. Kim, and G. R. Stewart, J. Low. Temp. Phys. **126**, 815 (2002).
- 5) Y. Shimizu, Y. Haga, Y. Ikeda, T. Yanagisawa, and H. Amitsuka, Phys. Rev. Lett. **109**, 217001 (2012).
- 6) J. P. Brison, J. Flouquet, and G. Deutscher, J. Low Temp. Phys. **76**, 453 (1989).
- 7) P. Gegenwart, C. Langhammer, R. Helfrich, N. Oeschler, M. Lang, J. S. Kim, G. R. Stewart, and F. Steglich, Physica C (Amsterdam, Neth.) **408-410**, 157 (2004).
- 8) Y. Shimizu, A. Pourret, G. Knebel, A. Palacio-Morales, and D. Aoki, Phys. Rev. B **92**, 241101(R) (2015).
- 9) H. R. Ott, H. Rudigier, T. M. Rice, K. Ueda, Z. Fisk, and J. L. Smith, Phys. Rev. Lett. **52**, 1915 (1984).
- 10) Y. Shimizu, D. Braithwaite, D. Aoki, B. Salce, and J-P. Brison, Phys. Rev. Lett. **122**, 067001 (2019).
- 11) S. Coad, A. Hiess, D. McMorro, G. H. Lander, G. Aeppli, Z. Fisk, G. Stewart, S. Hayden, and H. Mook, Physica B **276-278**, 764 (2000).
- 12) A. Hiess, R. H. Heffner, J. E. Sonier, G. H. Lander, J. L. Smith, and J. C. Cooley, Phys. Rev. B **66**, 064531 (2002).
- 13) A. Hiess, A. Schneidewind, O. Stockert, and Z. Fisk, Phys. Rev. B **89**, 235118 (2014).
- 14) A. Hiess, M. Bonnet, P. Burlet, E. Ressouche, J.-P. Sanchez, J. C. Waerenborgh, S. Zwirner, F. Wastin, J. Rebizant, G. H. Lander, and J. L. Smith, Phys. Rev. Lett. **77**, 3917 (1996).
- 15) F. Vigneron, M. Bonnet, J. Chappert, J. Phys. F: Met. Phys. **15**, 181 (1985).
- 16) P. Dervenagas, P. Burlet, M. Bonnet, F. Bourdarot, A. Hiess, S. L. Bud'ko, P. C. Canfield, G. H. Lander, J. S. Kim and G. R. Stewart, Phys. Rev. B **61**, 401 (2000).
- 17) F. Vigneron, M. Bonnet, A. Herr, and J. Schweizer, J. Phys. F: Met. Phys. **12**, 223 (1982).
- 18) G. Heinrich, J. P. Kappler, and A. Meyer, Phys. Lett. **74A**, 121 (1979).
- 19) A. P. Ramirez, B. Batlogg, and Z. Fisk, Phys. Rev. B **34**, 1795 (1986).
- 20) P. Bonville, P. Imbert, and G. Jehanno, J. Phys. F: Met. Phys. **16**, 1873 (1986).
- 21) G. v. Eynatten, C. F. Wang, N. S. Dixon, L. S. Fritz, S. S. Hanna, Z. Phys. B Condensed Matter **51**, 37 (1983).
- 22) K. H. Frank, B. Reihl, Z. Fisk, and G. Schmiester, J. Less-Common Metals, **111**, 251 (1985).
- 23) U. Walter, Z. Fisk, and E. Holland-Moritz, J. Mag. Mag. Mater. **47&48**, 159 (1985).
- 24) T. Sakakibara, H. Mitamura, T. Tayama, and H. Amitsuka, Jpn. J. Appl. Phys. **33**, 5067 (1994).
- 25) Y. Shimizu, Y. Kono, T. Sugiyama, S. Kittaka, Y. Shimura, A. Miyake, D. Aoki, and T. Sakakibara, Rev. Sci. Instrum. **92**, 123908 (2021).
- 26) G. Oomi, M. Ohashi, T. Sawamura, T. Kagayama, A. H. Lacerda, and J. L. Smith, Trans. Mang. Soc. **3**, 35-38 (2003).
- 27) Y. G. Naudyuk, O. E. Kvitnitskaya, K. Gloos, A. G. M. Jansen, P. Wyder, and Z. Fisk, Physica B **259-261** (1999).
- 28) P. M. Chaikin and T. C. Lubensky, *Principles of condensed matter physics*, Cambridge University Press (1995).
- 29) E. F. Bertaut Acta Cryst. **A24**, 217 (1968).
- 30) Y. A. Izyumov and V. E. Naish, J. Magn. Magn. Mater. **12**, 239 (1979).
- 31) Y. Kitano and T. Nagamiya: Prog. Theor. Phys. **31**, 1 (1964).
- 32) H. Hidaka, K. Mizuguchi, E. Hayasaka, T. Yanagisawa, J. Ohara, and H. Amitsuka, Phys. Rev. B **102**, 174408 (2020).
- 33) T. Komatsubara, T. Suzuki, and E. Hiraehara, J. Phys. Soc. Jpn. **28**, 317 (1970).
- 34) T. Sakakibara, S. Nakamura, S. Kittaka, M. Kakihana, M. Hedo, T. Nakama, and Y. Ōnuki, J. Phys. Soc. Jpn. **90**, 064701 (2021).
- 35) A. Bauer, A. Senyshyn, R. Bozhanova, W. Simeth, C. Franz, S. Gottlieb-Schönmeyer, M. Meven, T. E. Schrader, and C. Pfleiderer, Phys. Rev. Material **6**, 034406 (2022).
- 36) A. Nowack, S. Wasser, W. Schlabit, O. E. Kvitnitskaya, and Z. Fisk, Phys. Rev. B **56**, 14964 (1997).
- 37) M. J. Besnus, A. Braghta, N. Hamdaoui, and A. Meyer, J. Mag. Mag. Mat **104-107**, 1385 (1992).